A Novel Calibration Method of Short-Time Waveform Signals Passed through LTI Systems: 1. Methodology and Simple Examples

M. Kitahara[1*], S. Matsuda[2], Y. Katoh[3], H. Kojima[4], Y. Kasahara[2], Y. Miyoshi[1], S. Nakamura[1], and M. Hikishima[5]

[1]Institute for Space-Earth Environmental Research, Nagoya University, Nagoya, Japan

[2]Graduate School of Natural Science and Technology, Kanazawa University, Kanazawa, Japan

[3]Graduate School of Science, Tohoku University, Sendai, Japan

[4]Research Institute for Sustainable Humanosphere, Kyoto University, Kyoto, Japan

[5]Institute of Space and Astronautical Science/Japan Aerospace Exploration Agency, Kanagawa, Japan

Corresponding author: Masahiro Kitahara (kitahara.masahiro@isee.nagoya-u.ac.jp)

Key Points:

- We propose a novel calibration method using short-time Fourier transform for waveform data, such as plasma waves observed in space.
- The accuracy of the novel method is evaluated using the transfer functions of well-known filters and frequency-fixed sinusoidal waveforms.
- The novel method provides the most accurately calibrated data compared with conventional methods using short-time Fourier transform.

Abstract

We propose a novel and accurate calibration method for short-time waveform signals passed through a linear time-invariant (LTI) system that has a non-negligible group delay. Typically, the calibration process of waveform data is expressed by the Fourier transform and is performed in the frequency domain. If the short-time Fourier transform is applied to the waveform data in the calibration process, multiplying the data by a window function is highly recommended to reduce side-lobe effects. However, the multiplied window function is also modified in the calibration process. We analyzed the modification mathematically and derived a novel method to eliminate the modification of the multiplied window function. In the novel method, calibrated data in the frequency domain are inverse-transformed into waveform data at each frequency, divided by a modified window function at each frequency, and accumulated over the frequencies. The principle of this method derived quantitatively indicates that the calibration accuracy depends on the transfer function of the system, frequency resolution of the Fourier transform, type of the window function, and typical frequency of the waveform data. Compared with conventional calibration methods, the proposed method provides more accurate results in various cases. This method is useful for calibration of general radio wave signals through passed LTI systems as well as for calibration of plasma waves observed in space.

1 Introduction

Time-sequential signals are measured and analyzed for multi purposes in various scientific fields. The following are some typical examples of time-sequential signals: brain waves and electrocardiograms in medical science, acoustic signals and alternating current signals in engineering science, electromagnetic waves in physics, and seismic waves in geoscience. Particularly, in space exploration, many satellites have observed various types of electric and magnetic field waveforms to investigate and develop space plasma physics (e.g., Angelopoulos, 2008; Mauk et al., 2013; Burch et al., 2016; Miyoshi et al., 2018). Most of the signals are essentially continuous analog signals and include unexpected noises, such as rapid fluctuations and/or tardily varying offsets. To observe the signals quantitatively and convert them into discrete digital data, the signals should be detected by sensors, amplified using amplifiers, and passed through filters to eliminate noises. The sensors, amplifiers, filters, and other processor types, expressed as linear time-invariant (LTI) systems, serve expected functions; however, they also provide unintentional signal modification, such as gain changes and phase shifts. Removing the unintentional modification from output signals is called calibration, and the output signals are divided by the transfer function of the systems in the frequency domain, which is a conventional calibration method (Matsuda et al., 2021). Because time-sequential signals that should be calibrated typically comprise finite data points, the conventional calibration method is effective only when the number of data points is sufficiently large and the sampling frequency is much shorter than the typical frequencies of the observed signals. In some cases, however, the number of data points of the observed signals and/or the calculation resource should be limited, and dividing the signals by the transfer function alone is not sufficient for the calibration. For example, the Software-type Wave-Particle Interaction Analyzer (S-WPIA) (Katoh et al., 2018) aboard the Arase satellite (Miyoshi et al., 2018) requires onboard calibration processes for electromagnetic waveform data, and the calculation resources for each time window are limited to several hundred points (Hikishima et al., 2014; 2018).

In this paper, we focus on cases with short data sizes, such as a case where the short-time Fourier transform (STFT) algorithm is used, and we propose a novel calibration method for analog filters that have a non-negligible group delay. The methodology and principles are described in Section 2. The method for quantifying the accuracy of the calibration methods is presented in Section 3, and the example calibration result is presented in Section 4. Next, we discuss the relationship between the calculation time and resources, and the characteristics of each calibration method in Section 5.

2 Principle and Methodology

2.1 Main principle

Based on signal processing textbooks (e.g., Bendat & Piersol, 2010), the calibration process is expressed using the Fourier transform. Let x_{in} and x_{out} be input and output signals as functions of time t. The modification caused by a system is expressed by the convolution of a response of the system to an impulse $g(t)$ such as

$$x_{\mathrm{out}}(t) = g(t) * x_{\mathrm{in}}(t). \tag{1}$$

Let $\mathcal{F}$ and $\mathcal{F}^{-1}$ be the operations of the Fourier transform (FT) and the inverse Fourier transform (IFT) for a function, respectively; let $X(\omega)$ and $G(\omega)$ be $X(\omega) = \mathcal{F}[x(t)]$ and $G(\omega) = \mathcal{F}[g(t)]$, where ω is the angular frequency of the signals. Here, $G(\omega)$ represents the transfer function of the system. Because the convolution operation in the time domain is equivalent to multiplying a window in the frequency domain, equation (1) can be rewritten as

$$X_{\mathrm{out}}(\omega) = G(\omega) \cdot X_{\mathrm{in}}(\omega). \tag{2}$$

By introducing $\mathcal{C}$ operator as a sequence of operations that perform the FT of signals, dividing the signals $G(\omega)$ in the frequency domain, and then performing the IFT, such as

$$\mathcal{C}[f(x)] = \mathcal{F}^{-1}\left[\frac{\mathcal{F}\{x(t)\}}{G(\omega)}\right] = \mathcal{F}^{-1}\left[\frac{X(\omega)}{G(\omega)}\right], \tag{3}$$

the input signal $x_{\mathrm{in}}(t)$ can be ideally reproduced by the following process:

$$x_{\mathrm{in}}(t) = \mathcal{F}^{-1}\left[\frac{\mathcal{F}[x_{\mathrm{out}}(t)]}{G(\omega)}\right] = \mathcal{C}[x_{\mathrm{out}}(t)]. \tag{4}$$

In actual cases, the discrete Fourier transform (DFT) and the inverse discrete Fourier transform (IDFT) are commonly used in place of $\mathcal{F}$ and $\mathcal{F}^{-1}$ in equation (4) owing to the limited number of data points. Let t_n, f_s, N, and T be the detected time, the sampling frequency of the detected data, the number of data points, and the time duration of the data (the window size of the data), and let k, m, and n be index integers. Thus, DFT and IDFT are defined as

$$X(\omega_m) = \mathcal{F}_{\mathrm{D}}[x(t_n)] = \frac{1}{N}\sum_{n=0}^{N-1} x(t_n)\, e^{-i\omega_k t_n} = \frac{1}{N}\sum_{n=0}^{N-1} x(t_n)\, e^{-\frac{2\pi i m n}{N}}, \tag{5}$$

$$x(t_n) = \mathcal{F}_{\mathrm{D}}^{-1}[X(\omega_m)] = \sum_{k=0}^{N-1} X(\omega_m)\, e^{i\omega_k t_n} = \sum_{k=0}^{N-1} x(\omega_m)\, e^{\frac{2\pi imn}{N}}, \tag{6}$$

where $t_n = n\Delta t,\ \omega_m = m\Delta\omega = 2\pi m\Delta f,\ \Delta t = \frac{1}{f_s} = \frac{T}{N},\ \Delta f = \frac{f_s}{N}$. We define the operation $\mathcal{C}_D$ as the calibration method in (4) applied to discrete finite data with the DFT/IDFT expressed as

$$\mathcal{C}_D[x_{\mathrm{out}}(t_n)] = \mathcal{F}_D^{-1}\left[\frac{\mathcal{F}_D[x_{\mathrm{out}}(t_n)]}{G(\omega_m)}\right], \tag{7}$$

where $\mathcal{C}_D$ is the $\mathcal{C}$ operation using the DFT/IDFT for digital data. Note that, for the case where the frequency resolution $\Delta\omega$ (or Δf) is small, that is, the number of data points N is large, the calibration method described in (4) is reasonable for the estimation of input data with high accuracy. However, $x_{\mathrm{in}} \neq \mathcal{C}[x_{\mathrm{out}}]$ for finite N.

In typical DFT/IDFT processes, which include the STFT process, the data to be applied to the DFT/IDFT are multiplied by a window function to taper off to the edges and avoid side-lobe effects owing to discontinuity at the edges. Here, let $w(t_n)$ be a window function in the time domain. By applying the operation $\mathcal{C}_D$ to the tapered output data, we can estimate the input data using the following operation $\mathcal{C}_w$:

$$\mathcal{C}_w[x_{\mathrm{out}}(t_n), w(t_n)] = \frac{\mathcal{C}_D[w(t_n)\cdot x_{\mathrm{out}}(t_n)]}{w(t_n)} = \frac{\mathcal{F}^{-1}\left[\frac{\mathcal{F}[w(t_n)\cdot x_{\mathrm{out}}(t_n)]}{G(\omega_m)}\right]}{w(t_n)}. \tag{8}$$

The calibration process expressed by operation $\mathcal{C}_w$ is more accurate than $\mathcal{C}_D$ for a sufficiently large N because the side lobes become small in the frequency domain by edge tapering. However, the operation $\mathcal{C}_w$ cannot exactly reproduce the input data x_{in}. Let W be the spectrum of the window function in the frequency domain, expressed as $W(\omega) = \mathcal{F}[w(t)]$. The relation between the transfer function and tapered data in the time domain can be expressed as

$$w(t)\cdot x_{\mathrm{out}}(t) = w(t)\cdot\big(g(t) * x_{\mathrm{out}}(t)\big), \tag{9}$$

and its relation in the frequency domain is easily derived from equation (9) as

$$W(\omega) * X_{\mathrm{out}}(\omega) = W(\omega) * \big(G(\omega)\cdot X_{\mathrm{in}}(\omega)\big). \tag{10}$$

Based on equations (9) and (10), because the windowing and filtering processes are conjugate operations of each other, the convoluted window function in the frequency domain is also modified by the calibration process divided by the transfer function G in the frequency domain. This fact is also expressed as $x_{\mathrm{in}} \neq \mathcal{C}_w[x_{\mathrm{out}}]$ for finite N owing to $(W * (G\cdot X_{\mathrm{in}}))/G \neq W * F_{\mathrm{in}}$.

2.2 Modulation of window functions

In this section, to evaluate the difference between x_{in} and $\mathcal{C}_w[x_{\text{out}}]$, we quantify the unintentional modulation of window functions in the calibration process. First, we assume a simple case in which the output signals are expressed as a monotonic sinusoidal wave as

$$x_{\text{out}}(t_n) = A_0 e^{i(\omega_0 t_n + \phi_0)}, \tag{11}$$

where A_0, ϕ_0, and ω_0 are the amplitude, initial phase, and frequency of the waveform, respectively. The wave period of the signals is assumed as an integer multiple of the time width of the window ($\omega_0 = m_0 \Delta\omega$ with $m_0 \in \mathbb{N}$). Note that because $\Delta\omega$ is defined as $\Delta\omega = 2\pi/T$, $\Delta\omega$ represents not only the frequency resolution of the DFT/IDFT but also the fundamental frequency of the window function. In this case, by applying the DFT/IDFT described in (5) and (6), the frequency spectra of the output signals are succinctly expressed as

$$X_{\text{out}}(\omega_m) = A_0 e^{i\phi_0} \delta_{m,m_0}, \tag{12}$$

where $\delta_{i,j}$ is the Kronecker delta. Let $|G(\omega)|$ and $\theta(\omega)$ be the magnitude and argument of the complex transfer function $G(\omega)$ as written by $|G(\omega)| = \text{abs}\big(G(\omega)\big) = \sqrt{\text{Re}[G(\omega)]\ + \text{Im}[G(\omega)]}$ and $\theta(\omega) = \arg\big(G(\omega)\big) = \tan^{-1}(\text{Im}[G(\omega)]/\text{Re}[G(\omega)])$, where $\text{Re}[z]$ and $\text{Im}[z]$ are the real and imaginary parts of a complex number z, respectively. The operation $\mathcal{C}_D$ for the output signal without any window function can be rewritten as

$$\mathcal{C}_D[x_{\text{out}}(t_n)] = \mathcal{F}_D^{-1}\left[\frac{A_0 e^{i(\phi_0 - \theta(\omega_0))}}{|G(\omega_0)|}\delta_{m,m_0}\right] = \frac{A_0}{|G(\omega_0)|} e^{i(\omega_0 t_n + \phi_0 - \theta(\omega_0))}. \tag{13}$$

For general cases, the output signals $x_{\text{out}}(t_n)$ can be expanded by a series of exponential functions using DFT:

$$x_{\text{out}}(t_n) = \sum_{m=0}^{N-1} X_m e^{i\omega_m t_n}, \tag{14}$$

where $X_m = X(\omega_m) = \mathcal{F}_D[w(t_n)]$. The window function $w(t_n)$ can also be expanded as

$$w(t_n) = \sum_{k=0}^{N-1} W_k e^{ik\Delta\omega t_n}, \tag{15}$$

where $W_k = W(\omega_k) = \mathcal{F}_D[w(t_n)]$.

Assuming the condition of

$$W_{\frac{N}{2}} \ll W_0, \tag{16}$$

the following approximation can be derived from equation (15),

$$w(t_n) \simeq W_0 + \sum_{k=1}^{\frac{N}{2}-1} \left\{ W_k e^{ik\Delta\omega t_n} + W_{-k} e^{-ik\Delta\omega t_n} \right\}. \tag{17}$$

The right- and left-hand sides of approximation (17) should be exactly equivalent because $W_{\frac{N}{2}} = 0$ in the case of the window function expressed as a simple summation of the cosine function (e.g., the Hamming window, etc.). By multiplying both sides of equations (14) by (17), we obtain the following expression:

$$w(t_n) \cdot x_{\text{out}}(t_n) \simeq \sum_{m=0}^{N-1} X_m \left\{ W_0 e^{i\omega_m t_n} + \sum_{k=1}^{\frac{N}{2}-1} \left\{ W_k e^{i(\omega_m + k\Delta\omega)t_n} + W_{-k} e^{i(\omega_m - k\Delta\omega)t_n} \right\} \right\}. \tag{18}$$

The first term on the right-hand side of equation (18) mainly indicates a peak point of the main lobe of signals (including side lobes), and the other terms corresponding to the accumulation of k mainly indicate the main lobe expansion around the signal frequencies ($\sim \omega_m \pm k\Delta\omega$) (including side-lobe reduction parts). Here, we introduce the new parameters $W_{k,m}^{+}$, $W_{k,m}^{-}$, $\theta_{k,m}^{+}$, and $\theta_{k,m}^{-}$ with double sign in the same order as

$$W_{k,m}^{\pm} = \frac{|G(\omega_m)|}{|G(\omega_m \pm k\Delta\omega)|} W_{\pm k}, \tag{19}$$

$$\theta_{k,m}^{\pm} = \frac{\theta(\omega_m + k\Delta\omega) \pm \theta(\omega_m - k\Delta\omega)}{2}. \tag{20}$$

Using these parameters expressed as (19) and (20) and applying the description of operation $\mathcal{C}_D$ expressed as (13) to equation (18), the following expressions can be derived:

$$\begin{aligned}
&\mathcal{C}_D[w(t_n) \cdot x_{\text{out}}(t_n)] \\
&\simeq \sum_{m=0}^{N-1} X_m \left[\frac{W_0}{|G(\omega_m)|} e^{i(\omega_m t_n - \theta(\omega_m))} \right. \\
&\qquad \left. + \sum_{k=1}^{\frac{N}{2}-1} \left[\frac{W_k e^{i((\omega_m + k\Delta\omega)t_n - \theta(\omega_m + k\Delta\omega))}}{|G(\omega_m + k\Delta\omega)|} + \frac{W_{-k} e^{i((\omega_m - k\Delta\omega)t_n - \theta(\omega_m - k\Delta\omega))}}{|G(\omega_m - k\Delta\omega)|} \right] \right] \\
&= \sum_{m=0}^{N-1} \frac{X_m}{|G(\omega_m)|} \left\{ W_0 e^{i(\omega_m t_n - \theta(\omega_m))} \right. \\
&\qquad \left. + \sum_{k=1}^{\frac{N}{2}-1} \left[W_{k,m}^{+} e^{i\left((\omega_m + k\Delta\omega)t_n - (\theta_{k,m}^{+} + \theta_{k,m}^{-})\right)} + W_{k,m}^{-} e^{i\left((\omega_m - k\Delta\omega)t_n - (\theta_{k,m}^{+} - \theta_{k,m}^{-})\right)} \right] \right\}.
\end{aligned} \tag{21}$$

If we assume

$$\theta(\omega_m) \simeq \theta^+_{k,m}, \tag{22}$$

the condition (22) is equivalent to

$$\frac{1}{2}(k\Delta\omega)^2 \ll \frac{|\theta(\omega_m)|}{|\theta''(\omega_m)|} \quad (\text{for all } k) \tag{23}$$

because $\theta^+_{k,m}$ can be approximated using Taylor series expansion as

$$\theta^+_{k,m} = \frac{\theta(\omega_m + k\Delta\omega) + \theta(\omega_m - k\Delta\omega)}{2} = \theta(\omega_m) + \frac{1}{2}(k\Delta\omega)^2\theta''(\omega_m) + \cdots. \tag{24}$$

Under the condition of inequality (23), equation (21) can be rewritten as

$$\mathcal{C}_D[w(t_n)\cdot x_{\text{out}}(t_n)] \simeq \sum_{m=0}^{N-1}\left\{w_{\text{sh}}(t_n,\omega_m)\left(\frac{X_m}{|G(\omega_m)|}e^{i(\omega_m t_n - \theta(\omega_m))}\right)\right\}, \tag{25}$$

where

$$w_{\text{sh}}(t_n,\omega_m) = W_0 + \sum_{k=1}^{\frac{N}{2}-1}\left\{W^+_{k,m}e^{\{i(k\Delta\omega t_n - \theta^-_{k,m})\}} + W^-_{k,m}e^{-i(k\Delta\omega t_n - \theta^-_{k,m})}\right\}. \tag{26}$$

Introducing $\widetilde{W}^+_{k,m}$ and $\widetilde{W}^-_{k,m}$, respectively as

$$\widetilde{W}^{\pm}_{k,m} = W^+_{k,m} \pm W^-_{k,m}, \tag{27}$$

the expression (26) can be rewritten as

$$w_{\text{sh}}(t_n,\omega_m) = W_0 + \sum_{k=1}^{\frac{N}{2}-1}\left\{\widetilde{W}^+_{k,m}\cos\left(k\Delta\omega t_n - \theta^-_{k,m}\right) + i\widetilde{W}^-_{k,m}\sin\left(k\Delta\omega t_n - \theta^-_{k,m}\right)\right\}. \tag{28}$$

Consequently, we can derive $x_{\text{in}}(t_n) \neq \mathcal{C}_w[x_{\text{out}}(t_n)] = \mathcal{C}_D[w(t_n)\cdot x_{\text{out}}(t_n)]/w(t_n)$ because of $w(t_n) \neq w_{\text{sh}}(t_n,\omega_m)$ in (25). This unexpected discordance is mainly caused by the main lobe expansion shown in (18). The main lobe expansion terms are unintentionally divided by the transfer function at expanded frequencies ($\sim \omega_m \pm k\Delta\omega$), described as the second and third terms of equation (21), and it yields the unexpected modulation of the window function. Equation (28) shows that the amplitude of the window function is rotated and/or extended by $\widetilde{W}^+_{k,m}$ and $\widetilde{W}^-_{k,m}$ in the complex space, and the phase of the window function is shifted by $\theta^-_{k,m}$, which is the local linearity of the phase transfer function in the time domain. Because the approximations are established based on the assumptions expressed as inequalities (16) and (23), the approximations are reasonable when the following three conditions are satisfied:

- Condition A (for the window function): A sufficiently small K, which is defined as the maximum k satisfying $W_k \neq 0$, is required. That is, the window function should comprise low-order cosine functions. This condition also indicates that approximation (23) is not effective for the case of window functions that include high k components (e.g., the Gaussian window, the triangle window, the sine window (the half-cosine window), etc.)

- Condition B (for frequency resolution): A sufficiently small $\Delta\omega$ is required. That is, the sampling frequency f_s should be sufficiently high, and/or the data length N (or T) should be sufficiently large.

- Condition C (for the transfer function): A roughly small θ'' is required. That is, the transfer function of the system should be locally linear in the range of $\pm k\Delta\omega$. Note that the transfer function does not have a completely linear phase response in the frequency domain.

In extremely small $\Delta\omega$ cases (or large N), the factor $w_{\mathrm{sh}}(t_n, \omega_m)$ in the approximation (25) expressed as equation (26), which corresponds to the unintentionally modulated window function, are almost equal to the $w(t_n)$ expressed as equation (17) because $W_{k,m}^{\pm}$ and $\theta_{k,m}^{-}$ are approximately equal to $W_{\pm k}$ and 0, respectively. Therefore, the discordance between $\mathcal{C}_w[x_{\mathrm{out}}(t_n)]$ and $x_{\mathrm{in}}(t_n)$ is negligible. It should be noted that the accumulation in equation (25) cannot be replaced with the fast Fourier transform (FFT) algorithm because the modulation of the window function caused by operation $\mathcal{C}_D$ occurs at each frequency in the frequency domain.

2.3 Various window functions

In the previous section, we derived the discordance between $\mathcal{C}_w[w(t_n) \cdot x(t_n)]$ and $x_{\mathrm{in}}(t_n)$, and the discordance also depends on the type of window function. In this section, we focus on the dependency of the modulation characteristics on the types of window functions.

One of the most common window functions is the cosine-sum window. The cosine-sum window functions are represented as (e.g., Harris, 1978; Nuttall, 1981)

$$w_{\cos}(t_n) = \sum_{k=0}^{K} (-1)^k a_k \cos(k\Delta\omega t_n), \tag{29}$$

where K is the order of the cosine-sum window. $K = 0, a_0 = 1$ corresponds to the rectangular window with no window function, $K = 1, a_0 = 0.5, a_1 = 0.5$ corresponds to the Hann window (Hann, 1903; Blackman & Tukey, 1958), $K = 1, a_0 = 0.54, a_1 = 0.46$ corresponds to the Hamming window (Tukey & Hamming, 1949; Blackman & Tukey, 1958), $K = 2, a_0 = 0.42, a_1 = 0.5, a_2 = 0.08$ corresponds to the Blackman window (Blackman & Tukey, 1958), and $K = 3, a_0 = 0.35875, a_1 = 0.48829, a_2 = 0.14128, a_3 = 0.01168$ corresponds to the Blackman-Harris window (Harris, 1978). Figures 1a and 1b show these window functions in the

time domain and magnitude properties in the frequency domain. The black, red, yellow, green, and blue lines correspond to the rectangular, Hamming, Hann, Blackman, and Blackman-Harris window, respectively. It is well known that larger-K cosine-sum window functions have a wider main lobe and lower-level side lobes.

Tukey (1967) introduced a cosine taper window, also known as the Tukey window, which is represented as

$$w_{\mathrm{Tk}}(t_n) = \begin{cases} 0.5 - 0.5\cos\dfrac{\Delta\omega t_n}{T_{\mathrm{S}}} & (0 < t_n < T_{\mathrm{S}}) \\ 1 & (T_{\mathrm{S}} \le t_n \le T_{\mathrm{S}} + T_{\mathrm{F}}) \\ 0.5 - 0.5\cos\dfrac{\Delta\omega(T_w - t_n)}{T_{\mathrm{S}}} & (T_{\mathrm{S}} + T_{\mathrm{F}} < t_n < T_w) \end{cases} \tag{30}$$

where T_{S}, T_{F}, and T_{w} are the time length of the slope regions, the flat top region length, and the whole window size ($T_w = 2T_{\mathrm{S}} + T_{\mathrm{F}}$), respectively. The cases where $T_{\mathrm{F}} = 0$ and $T_{\mathrm{F}} = T_w$ correspond to the Hann window and rectangular window, respectively. Because the Tukey window has a flat top region at the center of the window, the effect caused by the phase shift and amplitude rotation of a window function is negligible at the flat center region, similar to the rectangular window. Furthermore, the side-lobe effect is smaller than that of the rectangular window because of the tapered slope regions at both edges of the window. To reduce the side-lobe effects more than that of the Tukey window, including the merit of the rectangular window, we define the "Tukey-type" windows by combining the Tukey window and the cosine-sum windows as

$$w_{\mathrm{Tc}}(t) = \begin{cases} \displaystyle\sum_{k=0}^{N} (-1)^k a_k \cos\left(\frac{k\Delta\omega t_n}{T_s}\right) & (0 < t_n < T_{\mathrm{S}}) \\ 1 & (T_{\mathrm{S}} \le t_n \le T_{\mathrm{S}} + T_{\mathrm{F}}) \\ \displaystyle\sum_{k=0}^{N} (-1)^k a_k \cos\left(\frac{k\Delta\omega(T_w - t_n)}{T_s}\right) & (T_{\mathrm{S}} + T_{\mathrm{F}} < t_n < T_w) \end{cases} \tag{31}$$

For example, if we choose the Hamming window as a tapering curve, we can define the Tukey-Hamming window as

$$w_{\mathrm{TH}}(t) = \begin{cases} 0.54 - 0.46\cos\dfrac{\Delta\omega t_n}{T_{\mathrm{S}}} & (0 < t_n < T_{\mathrm{S}}) \\ 1 & (T_{\mathrm{S}} \le t_n \le T_{\mathrm{S}} + T_{\mathrm{F}}) \\ 0.54 - 0.46\cos\dfrac{\Delta\omega(T_w - t_n)}{T_{\mathrm{S}}} & (T_{\mathrm{S}} + T_{\mathrm{F}} < t_n < T_w) \end{cases} \tag{32}$$

Figures 1c and 1d show the time and frequency properties of four types of Tukey-type window functions and a rectangular window function with the same length of the flat region ($r = T_{\mathrm{F}}/T_{\mathrm{W}} = 0.3$). The black, red, yellow, green, and blue lines correspond to the rectangular, Tukey-Hamming, Tukey-Hann, Tukey-Blackman, and Tukey-Blackman-Harris window,

respectively. Because the phase shift effect described in the previous section results from the expanded main lobe, the Tukey-Hamming window should be one of the most useful windows in the displayed Tukey-type windows in Figures 1c and 1d. Figures 1e and 1f show the time and frequency properties of the Tukey-Hamming windows for different lengths of the flat region. The red, yellow, green, cyan, blue, and black lines correspond to $r = 0, 0.2, 0.4, 0.6, 0.8,$ and 1, respectively. Note that $r = 0$ and 1 correspond to the normal Hamming window and the rectangular window, respectively. The longer flat region makes higher side lobes around the main lobe like the rectangular window; therefore, the parameter roughly within $0.2 < r < 0.6$ seems useful for the calibration process.

Based on the above discussion and the description, two types of processes are conceivable as accurate waveform calibration with a window function: (1) Use a Tukey-type (particularly, Tukey-Hamming) window function to reduce side lobes, and (2) use a low-order cosine-sum window function and estimate the modification of a window function at each frequency. The latter method is presented in the previous section, and here, we describe a method specific to the first-order cosine-sine sum window functions.

In the case of the first-order cosine-sine sum window function (e.g., Hann window, Hamming window, etc.), the window function is expressed as

$$w_1(t_n) = a_0 - a_1 \cos(\Delta\omega t_n)\,, \tag{33}$$

$$w_1(t_n) = a_0 - \frac{a_1}{2} e^{i\Delta\omega t_n} - \frac{a_1}{2} e^{-i\Delta\omega t_n}, \tag{34}$$

and substituting (34) and (27) in (19) and (20), respectively, we can replace the following expression:

$$\widetilde{W}^{\pm}(\omega) = -\frac{a_1}{2}\left\{\frac{|G(\omega)|}{|G(\omega+\Delta\omega)|} \pm \frac{|G(\omega)|}{|G(\omega-\Delta\omega)|}\right\}, \tag{35}$$

$$\theta^{\pm}(\omega) = \frac{\theta(\omega+\Delta\omega) \pm \theta(\omega-\Delta\omega)}{2}. \tag{36}$$

Using (35) and (36), the modulated window function (28) is rewritten as

$$w_{\mathrm{sh1}}(t_n, \omega_m) = a_0 + \widetilde{W}_m^{+} \cos(\Delta\omega t_n - \theta_m^{-}) + i\widetilde{W}_m^{-} \sin(\Delta\omega t_n - \theta_m^{-})\,. \tag{37}$$

where $\widetilde{W}_m^{\pm} = \widetilde{W}^{\pm}(\omega_m)$, and $\theta_m^{-} = \theta^{-}(\omega_m)$. Based on the above, we propose a novel method to calibrate the waveform accurately with the first-order cosine-sine sum window function, written as

$$x_{\mathrm{in}}(t_n) \simeq \sum_{m=0}^{N-1} \frac{1}{w_{\mathrm{sh1}}(t_n, \omega_m)} \cdot \frac{\mathcal{F}_D[w_1(t_n) \cdot x_{\mathrm{out}}(t_n)] e^{i(\omega_m t_n - \theta(\omega_m))}}{|G(\omega_m)|}. \tag{38}$$

Note that the first-order cosine-sum window functions automatically satisfy condition A described in the previous section; however, conditions B and C are still required for the

approximation. Under these conditions, we can use any type of window function such as a high-order cosine-sum window function by substituting $W_{\pm k}$ into $(-1)^k a_k/2$ and replacing $w_{\mathrm{sh1}}(t_n, \omega_m)$ by $w_{\mathrm{sh}}(t_n, \omega_m)$ in equation (28).

2.4 List of calibration methods

Figure 2 summarizes the flowcharts of the conceivable calibration procedures for the STFT cases. The details of the methods are as follows:

2.4.1 Method 1

Method 1 processes are shown with yellow arrows in Figure 2. The split data for STFT are not multiplied by any window function (or multiplied by a rectangular window as a window function), the data are calibrated in the frequency domain, and the calibrated short-time data are connected in the time domain. The sequence of these processes, except for splitting and merging, can be described as the operation $\mathcal{C}al_1$ expressed as

$$\mathcal{C}al_1[x_{\mathrm{out}}(t_n)] = \mathcal{C}_D[x_{\mathrm{out}}(t_n)] = \mathcal{F}_D^{-1}\left[\frac{\mathcal{F}_D[x_{\mathrm{out}}(t_n)]}{G(\omega_m)}\right]. \tag{39}$$

In the case where the typical wave period of the signals comprises integer multiples of the time width of the STFT time window or in the case where the number of data points in the STFT time window is sufficiently large, the calibrated signals are ideally identical to the input signals. Conversely, when the typical wave period of the signals is not expressed by integers or half-integer multiples of the time width of the window, the calibrated signals significantly disagree with the input signals owing to side-lobe effects in the DFT process.

2.4.2 Method 2

Method 2 processes are shown with green arrows in Figure 2. Split data for STFT are multiplied by a cosine-sum window in the time domain and calibrated in the frequency domain. The calibrated short-time data inverse-transformed into waveforms in the time domain are divided by the window function, and subsequently the data are connected in the time domain. A sequence of the processes, except for splitting and merging, can be described as the operation $\mathcal{C}al_2$ expressed as

$$\mathcal{C}al_2[x_{\mathrm{out}}(t_n)] = \mathcal{C}_w[x_{\mathrm{out}}(t_n), w(t_n)] = \frac{\mathcal{F}^{-1}\left[\frac{\mathcal{F}[w(t_n)\cdot x_{\mathrm{out}}(t_n)]}{G(\omega_m)}\right]}{w(t_n)}. \tag{40}$$

In this study, the Hamming window was used as $w(t_n)$ in the Method 2 process.

The side-lobe effects can be drastically reduced by the window function compared to the data calibrated by Method 1; however, the main lobe expansion effect is not negligible except for the case of sufficiently large data points.

2.4.3 Method 3

Method 3 processes are shown with blue arrows in Figure 2. Split data for STFT are multiplied by a Tukey-type window function (especially, a Tukey-Hamming window is useful) in the time domain and calibrated in the frequency domain. The calibrated short-time data inverse-transformed into waveforms in the time domain are divided by the window function; subsequently, the calibrated data are connected in the time domain. A sequence of the processes, except for splitting and merging, can be described as operation $\mathcal{C}al_3$ expressed as

$$\mathcal{C}al_3[x_{\mathrm{out}}(t_n)] = \mathcal{C}_w[x_{\mathrm{out}}(t_n), w_{\mathrm{TH}}(t_n)] = \frac{\mathcal{F}^{-1}\left[\frac{\mathcal{F}[w_{\mathrm{TH}}(t_n)\cdot x_{\mathrm{out}}(t_n)]}{G(\omega_m)}\right]}{w_{\mathrm{TH}}(t_n)}, \tag{41}$$

where w_{TH} is the Tukey-Hamming window, described in (32). The difference between Method 2 and Method 3 is only a window function used in the processes.

The side-lobe effects can be roughly reduced by the tapering sections of the Tukey-type window function compared to the data calibrated by Method 1, and the main lobe expansion effect is also reduced by the flat section of the Tukey-type window function compared to the data calibrated using Method 2.

2.4.4 Method 4 (a novel method)

Method 4 is a novel proposed method, shown with a red line flow in Figure 2. Split data for STFT are multiplied by a cosine-sum window in the time domain, and the transformed data are calibrated in the frequency domain, as in Method 2. The calibrated spectral data are inverse-transformed into waveforms in the time domain at each frequency, and in parallel, the modulated window functions are estimated at each frequency using (28) or (37). The calibrated waveforms at each frequency are divided by the estimated window functions at each frequency, respectively, and accumulated over all frequencies. The accumulated waveforms are connected in the time domain. A sequence of the processes except for splitting and merging can be described as operation $\mathcal{C}al_4$ expressed as

$$\mathcal{C}al_4[x_{\mathrm{out}}(t_n)] = \sum_{m=0}^{N-1} \frac{1}{w_{\mathrm{sh}}(t_n,\omega_m)} \cdot \frac{\mathcal{F}_D[w(t_n)\cdot x_{\mathrm{out}}(t_n)]e^{i(\omega_m t_n - \theta(\omega_m))}}{|G(\omega_m)|}, \tag{42}$$

where w and w_{sh} are the applied and estimated window functions, respectively, and w_{sh} is calculated using (28) and (37). In this study, the Hamming window is used for w such as w_1 shown in (33), and w_{sh} is calculated by w_{sh1}, which is described in (35), (36), and (37).

The side-lobe effects are significantly reduced by the window function, similar to the data calibrated by Method 2, and the main lobe expansion effect is also drastically eliminated by the estimation of the modulation of the window function. However, we cannot apply the FFT for the IDFT process, and we should perform the accumulation in (42) manually. The accumulation can also be interpreted as a manual deconvolution in the time domain. Therefore, the calculation time is much longer (it takes about $\mathcal{O}(N^2)$) than that of the other methods (corresponding to

354 $\mathcal{O}(\frac{1}{2}N\log_2 N)$).

355

356 ## 3 Evaluation Method

357 To evaluate our proposed method (Method 4) and the other three calibration methods
358 described in Section 2.4.4., we perform the test calibration using low-pass filters and sinusoidal
359 waveform data as the processing system and signals, respectively.

360

361 ### 3.1 Low-pass filters

362 We evaluated the calibration methods using three types of analog low-pass filters as the
363 processing system: a first-order RC filter, a Butterworth filter, and a Bessel filter. The transfer
364 function of the first-order RC filter (RC1) is the simplest low-pass filter and is expressed as

365 $$G_{\mathrm{RC1}}(f) = \frac{G_0}{1 + \frac{f}{f_{\mathrm{cutoff}}}i}. \tag{43}$$

366 Here, f_{cutoff} and G_0 are the cutoff frequency and offset value corresponding to the DC gain,
367 respectively.

368 A Butterworth filter (Butterworth, 1930) is designed as a filter with a maximally steep cutoff
369 property. The transfer function of the l-th order Butterworth filter is expressed as

370 $$G_{\mathrm{BW}l}(f) = \frac{G_0}{P_l^{\mathrm{BW}}\left(\frac{f}{f_{\mathrm{cutoff}}}i\right)}. \tag{44}$$

371 Here, $P_l^{\mathrm{BW}}(s)$ is the l-th degree Butterworth polynomial for complex variable s expressed as

372 $$P_l^{\mathrm{BW}}(s) = \begin{cases} \prod_{k=1}^{\frac{l}{2}}\left[s^2 - 2s\cos\left(\frac{2k+l-1}{2l}\pi\right) + 1\right] & \text{for even } n, \\ (1+s)\prod_{k=1}^{\frac{l-1}{2}}\left[s^2 - 2s\cos\left(\frac{2k+l-1}{2l}\pi\right) + 1\right] & \text{for odd } n. \end{cases} \tag{45}$$

373 A Bessel filter (Kiyasu, 1943; Thomson, 1949) was designed as a filter with a maximally linear
374 phase response. The transfer function of the l-th order Bessel filter is expressed as

$$G_{\mathrm{BS}l}(f) = \frac{G_0 P_l^{\mathrm{BS}}(0)}{P_l^{\mathrm{BS}}\left(\frac{f}{f_{\mathrm{cutoff}}} i\right)}. \tag{46}$$

Here, $P_l^{\mathrm{BS}}(s)$ is the l-th degree reverse Bessel polynomial represented as

$$P_l^{\mathrm{BS}}(s) = \sum_{k=0}^{l} \frac{(2l-k)!}{2^{l-k} k!\,(l-k)!} s^k\,. \tag{47}$$

Note that both a first-order Butterworth filter and a first-order Bessel filter correspond to the first-order RC filter.

Figure 3 shows the properties of the filters with $f_{\mathrm{cutoff}} = 10$ kHz and $G_0 = 1$. (a) and (e) are the amplitude components of the transfer function $|G(f)|$ corresponding to the gain of the filters; (b) and (f) are the phase components of the transfer function $\theta(f)$, and (c) and (g) are the first-order derivatives of $\theta(f)$, and (d) and (h) are the second-order derivatives of $\theta(f)$, respectively. The black, red, and blue lines correspond to the RC1, Butterworth, and Bessel filters, respectively, and the dashed and solid lines of the red and blue lines correspond to the third- and seventh-order filters, respectively. Figures 3a to 3d are plotted in the frequency range of 10^2 to 10^6 Hz with a logarithmic scale, and (e) to (h) are plotted in the frequency range of 0 to 10 kHz with a linear scale. The Butterworth filters have a flat magnitude at the passband and a steep slope at the cutoff frequency (red lines in Figure 3a) in exchange for a large phase delay at the passband (red lines in Figures 3b and 3f). The higher-order Butterworth filters provide a steeper gain cutoff and larger phase delays around the cutoff frequency. In contrast, the gain cutoff slopes of the Bessel filters are softer than those of Butterworth filters (blue lines in Figure 3a); however, the phase response is a gentle slope, such as a linear slope, and the slope does not depend on the order of the filter (blue lines in Figures 3b and 3c). θ' shown in Figures 3c and 3g indicate phase delays and also correspond to the phase shift of a window function described as θ^- in equations (28) and (37).

3.2 Test sinusoidal waves

The test waveform signals $x_{\mathrm{in}}(t_n)$ at each (arbitrary) frequency f_{in} are expressed as

$$x_{\mathrm{in}}(t_n) = A_{\mathrm{in}} \cos\left(\phi_{\mathrm{in}}(t_n, f_{\mathrm{in}})\right), \tag{48}$$

where

$$\phi_{\mathrm{in}}(t_n, f_{\mathrm{in}}) = 2\pi f_{\mathrm{in}} t_n + \phi_0. \tag{49}$$

Here, A_{in} and ϕ_0 are the constant wave amplitude and initial phase, respectively. Note that the suffix ‘out’ represents the calibration target. The signal output from the processing system corresponds to the signals inputted into the calibration processes. The suffix ‘in’ represents data, and the signals inputted into a processing system corresponding to the signal output from the

calibration process. The ideal output signals are represented as

$$x_{\mathrm{out}}(t_n) = A_{\mathrm{out}} \cos\big(\phi_{\mathrm{out}}(t_n, f_{\mathrm{out}})\big) = |G(f_{\mathrm{in}})| A_{\mathrm{in}} \cos\big(\phi_{\mathrm{in}} + \theta(f_{\mathrm{in}})\big) \tag{50}$$

To evaluate the accuracy of these calibration processes, we set $x_{\mathrm{out}}(t_n)$ as sinusoidal waves at first, and subsequently, we compared "the correct answer" expressed as $\frac{A_{\mathrm{out}}}{|G(f_{\mathrm{in}})|}\cos\big(\phi_{\mathrm{out}} - \theta(f_{\mathrm{in}})\big)$ and calibrated data $\mathcal{C}al_h[x_{\mathrm{out}}(t_n)]$ using the following indexes.

3.3 Evaluation parameters

We define three indexes: the maximum gap Γ, the error of amplitude Q, and the phase difference D. First, we define δ_h as a simple difference between the ideal signal $x_{\mathrm{in}}(t_n)$ and calibrated signal $\mathcal{C}al_h[x_{\mathrm{out}}(t_n)]$ expressed as

$$\delta_h(t_n) = \mathcal{C}al_h[x_{\mathrm{out}}(t_n)] - x_{\mathrm{in}}(t_n). \tag{51}$$

Note that the suffix h represents the method number corresponding to Method 1, 2, 3, or 4. Using δ_h, we define the maximum gap Γ as

$$\Gamma_h = \max_{T_c - T_a \le t_n \le T_c + T_a} \left(\frac{|\delta_h(t_n)) - \delta_h(t_{n-1})|}{A_{\mathrm{in}}} \right) \times 100\ [\%] \tag{52}$$

The maximum gap Γ mainly shows how seamless the joint section of the STFT data windows is. Next, we define the error of the amplitude Q, and the phase difference D calculated by the instantaneous amplitude and phase. The instantaneous amplitude $\mathcal{A}_{\mathrm{inst}}$ and the instantaneous phase $\mathcal{P}_{\mathrm{inst}}$ for general $x(t_n)$ can be respectively derived using the Hilbert transform as

$$\mathcal{A}_{\mathrm{inst}}[x(t_n)] = \sqrt{\big(x(t_n)\big)^2 + (\mathcal{H}_D[x(t_n)])^2} \tag{53}$$

$$\mathcal{P}_{\mathrm{inst}}[x(t_n)] = \arg(x(t_n) + i\mathcal{H}_D[x(t_n)]) \bmod 2\pi \tag{54}$$

Here, the discrete Hilbert transform $\mathcal{H}_D$ is expressed as

$$\mathcal{H}_D[x(t_n)] = \mathrm{Re}\left[\mathcal{F}_D^{-1}[\tilde{X}(\omega_m)]\right] \tag{55}$$

$$X(\omega_m) = \mathcal{F}_D[x(t_n)] \quad \text{and} \quad \tilde{X}(\omega_m) = \begin{cases} X(\omega_m) & \text{for } m = 0 \text{ and } \dfrac{N}{2}, \\ 2X(\omega_m) & \text{for } 0 < m < \dfrac{N}{2}, \\ 0 & \text{for } m > \dfrac{N}{2}. \end{cases} \tag{56}$$

By using $\mathcal{A}_{\mathrm{inst}}$ and $\mathcal{P}_{\mathrm{inst}}$, We define the error of calibrated amplitude Q at each t_n as

$$Q_h(t_n) = \frac{\left|\mathcal{A}_{\mathrm{inst}}\left[\mathcal{C}al_h[x_{\mathrm{out}}(t_n)]\right] - A_{\mathrm{in}}\right|}{A_{\mathrm{in}}} \times 100\ [\%] \tag{57}$$

Because the instantaneous amplitude is not accurate around the edge of the data owing to the discontinuity effect of the DFT, we define the averaged error of the amplitude around the center area to avoid edge effects:

$$\bar{Q}_h = \underset{T_c - T_a \le t_n \le T_c + T_a}{\mathrm{avg}} \left(Q_h(t_n)\right)\ [\%], \tag{58}$$

where T_c is the center of data $x_{\mathrm{out}}(t_n)$ or $x_{\mathrm{in}}(t_n)$ expressed as $T_c = T_{\mathrm{total}}/2$ and T_a is the accumulation time width. In this study, we used $T_a = T_{\mathrm{total}}/10$.

We also define the phase difference using the instantaneous phase calculated from the Hilbert transform represented as

$$D_h(t_n) = \left|\mathcal{P}_{\mathrm{inst}}\left[\mathcal{C}al_h[x_{\mathrm{out}}(t_n)]\right] - \phi_{\mathrm{in}}(t_n)\right|\ [\mathrm{degree}] \tag{59}$$

We also define the averaged phase difference around the center area to avoid the edge effect represented as

$$\bar{D}_h = \underset{T_c - T_a \le t_n \le T_c + T_a}{\mathrm{avg}} \left(D_h(t_n)\right)\ [\mathrm{degree}]. \tag{60}$$

$\bar{Q}$ and $\bar{D}$ indicate the averaged accuracy of the calibration process.

We calculated these parameters for the five types of filters, the five combinations of N_{window} and N_{slide} for sufficiently large N_{total} at each frequency in the frequency range from 0 kHz to $f_{\mathrm{cutoff}} = 10$ kHz. Here, N_{window}, N_{slide}, and N_{total} are the number of window widths, sliding length of the window, and total data length corresponding to T_{total} shown in Figure 4. To make the discrete Hilbert transform sufficiently accurate, we chose $N_{\mathrm{total}} = 10{,}000$ points and $f_s = 100$ kHz.

4 Result and Discussion

Figure 5 shows a set of sample plots of (a) $\mathcal{C}al_h[x_{\mathrm{out}}(t_n)]$, (b) δ_h, (c) $Q_h(t_n)$, and (d) $D_h(t_n)$ around the center of the data. The yellow, green, blue, and red points and lines correspond to Method 1, 2, 3, and 4, respectively. To calculate this plot, we use the third-order Butterworth filter and 5.17 kHz sinusoidal waveform data with 10,000 points data corresponding to 0.1 s. The window width of the STFT and the sliding width were 128 and 64 points, respectively, and the sampling frequency was 100 kHz. The calibrated signals in Figure 5a can reproduce the input waveform; however, these results do not correspond to "the answer" exactly. Figure 5b shows the simple difference between the calibrated data and "the answer". We can recognize a non-negligible inaccuracy in Methods 1 and 2 and discontinuities at joint sections, which exist in the center of the displayed time duration, in Methods 1, 2, and 3. Figures 5c and

5d show the instantaneous accuracies of the amplitude and phase, respectively. Whereas Methods 1 and 2 include several to 10 percent errors in the calibrated amplitudes and several degrees in the calibrated phases, the calibration errors of the amplitudes and phases in Methods 3 and 4 are smaller than those of the other methods. However, the calibration result of Method 3 still contains non-negligible errors that reach several to 10 percent and degrees around joint sections caused by the discontinuities.

To reveal the general tendency, we performed the same test calibration for each frequency, window function, and window size. Figures 6, 7, 8, and 9 show the frequency dependences of the maximum gap Γ_h, the averaged error of amplitude $\bar{Q}_h$, and the phase difference $\bar{D}_h$. Overall, Methods 1 and 2 provide less accurate calibration results, and Methods 3 and 4 provide more accurate results.

The plots in Figures 6 and 7 are constructed using the same window functions (the third-order Butterworth filter) and different N_{window} and N_{slide}. Overall, the results are accurate in the order of Methods 4, 3, 2, and 1. For the cases of $N_{\mathrm{window}} = 128$, because the frequency resolution Δf corresponds to 512 Hz, Method 1 provides the most accurate data at frequencies equal to integer multiples of the frequency resolution ($f = m_0 \Delta f$ with $m_0 \in \mathbb{N}$) in the results provided by the four methods. However, Method 1 also provides the worst accurate data at the other frequencies, and its accuracy does not depend on the sliding number N_{slide}. Method 2 provides less accurate data, similar to Method 1. The frequency dependency of the gaps and errors in Method 2 was roughly flat. Methods 3 and 4 provide smaller errors compared to Methods 1 and 2, and the results from Method 3 still contain gaps. At lower frequencies that are smaller than approximately 1.5 kHz corresponding to three waves (sequences of up and down) in a window, the errors are larger than those at middle frequencies because side-lobe effects and a window function modulation effect cannot be estimated with sufficient accuracy owing to a few waves in a window. At higher frequencies, larger than approximately 8 to 9 kHz, the errors are also larger than those at middle frequencies because the signal frequencies are closer to the cutoff frequency and the second derivatives of the phase transfer function are larger than those at the middle frequencies. Decreasing the slide points (such as Figures 6a, 6b, and 6c in that order) and increasing the window width (such as Figures 7a, 7b, and 7c in that order) increases the accuracy of the results. Increasing the window width also contributes to increasing the accuracy of middle-frequency regions and reducing inaccurate low- and high-frequency regions.

Figures 8 and 9 show the dependence of the filters on the transfer function. Because the first-order RC filter and Bessel filters shown in Figure 8 with any order have almost the same phase properties, so-called maximally linear phase responses (black and blue lines in Figure 3), the calculation errors caused by all methods represent almost the same properties. Comparing Figures 9a, 9b, and 9c, the calibration results from the higher-order Butterworth filter tend to include larger gaps and errors owing to the larger second derivatives of the phase transfer functions (red lines in Figure 3). However, the results from Method 4 are still the most accurate among the results of the four methods with several times of 10^{-1} percent gaps and errors and several times of 10^{-1} degrees of phase errors. Summarily, Method 4 is the most accurate calibration procedure for the four conceivable methods, and the method conspicuously exhibits its potential for a small data point (i.e., short-time width) case and a more curved phase transfer function case.

In the case of the calculation time, let N_{split} be the number of times of splitting data and executing the FT process, and N_{split} be expressed by N_{total}, N_{window}, and N_{slide} as $N_{\mathrm{split}} = (N_{\mathrm{total}} - N_{\mathrm{window}})/N_{\mathrm{slide}} + 1 \simeq N_{\mathrm{total}}/N_{\mathrm{slide}}$ for $N_{\mathrm{total}} \gg N_{\mathrm{window}}, N_{\mathrm{slide}}$. The calculation times of the calibration process with Methods 3 and 4, τ_3 and τ_4 can be expressed as $\tau_3 \simeq (N_{\mathrm{total}} \times N_{\mathrm{window}} \times \log_2 N_{\mathrm{window}})/(2N_{\mathrm{slide}})$ and $\tau_4 \simeq N_{\mathrm{total}} \times N_{\mathrm{window}}^2/N_{\mathrm{slide}}$, respectively. For example, if we choose $N_{\mathrm{window}} = 2048$, $N_{\mathrm{slide}} = 2$ for Method 3, and $N_{\mathrm{slide}} = N_{\mathrm{window}}/2$ for Method 4, the calculation times for Methods 3 and 4 are roughly the same. Method 4 yields a more accurate calibration; however, it requires more calculation times than Method 3.

The proposed method is effective for more curved phase transfer function cases such as the case of a filter containing a steep slope and should be applied not only to filter calibration but also to other transfer functions that do not have linear phase characteristics (e.g., amplifier, sensor, etc.). The qualitative tendencies of the three conventional methods and the proposed method are summarized in Table 1. Note that each method has benefits and inexpediences, and which method should be chosen is a matter of degree of data accuracy, depending on the scientific/engineering purpose and practical use.

5 Summary

In this paper, we describe the behavior of window functions in the conventional calibration processes of waveform data passed through LTI systems, and we propose a novel calibration method described in Section 2.4.4. The essential process of the novel method is to estimate the unexpected modification of a window function in the calibration process and correcting it at each frequency in the time domain. The novel method provides sufficiently accurate calibration results without any change in the transfer function itself, even for short-time data cases, such as the case in which the STFT algorithm is used. We also clarified mathematically and quantitatively why using the Tukey-type window (Method 3), which has been used empirically, provides more accurate calibration results compared to Method 2. The calculation time of the novel method is much longer than that of the other methods because the FFT algorithm cannot be used in the inverse-transform process of the novel method. Which method should be chosen is a matter of degree of data accuracy and the calculation resource depending on the scientific/engineering purpose and practical use. As the next step of this study, we will apply this method to electromagnetic waveform data at VLF frequency range observed by the Plasma Wave Experiment/Waveform Capture (Kasahara et al., 2018; Matsuda et al, 2018) aboard the Arase satellite and evaluate the accuracy and usability of our proposed method.

Acknowledgments

No datasets were used in this work, and all data in the figures can be reproduced from the description and equations in the present study. This study was supported by Grants-in-Aid for Scientific Research (17H00728, 18H03727, 20H01959, 20K14546, and 21K13979) of the Japan Society for the Promotion of Science (JSPS) and JSPS-CAS bilateral project (JPJSBP10192504). This research was also supported by the "Computational Joint Research Program (Collaborative Research Project on Computer Science with High-Performance Computing)" at the Institute for Space-Earth Environmental Research, Nagoya University.

References

Angelopoulos, V. (2008), The THEMIS Mission. *Space Science Reviews, 141*, 5–34. https://doi.org/10.1007/s11214-008-9336-1

Bendat, J. S., & Piersol, A. G. (2011), Random data: analysis and measurement procedures (4th ed.). New York, NY: Wiley.

Blackman, R.B., & J. W. Tukey (1958), The measurement of power spectra: from the point of view of communications engineering. New York, NY: Dover Publications.

Burch, J. L., Moore, T. E., Torbert, R. B., & Giles, B. L. (2013), Magnetospheric Multiscale Overview and Science Objectives. *Space Science Reviews, 199*, 5–21. https://doi.org/10.1007/s11214-015-0164-9

Butterworth, S. (1930), On the Theory of Filter Amplifiers. *Experimental Wireless and the Wireless Engineer*, 7, 536–541.

Hann, J. V. (1903), *Handbook of Climatology*. London, Macmillan and Co., Ltd.

Harris, F. J. (1978), On the use of windows for harmonic analysis with the discrete Fourier transform. *Proceedings of the IEEE*, *66*(1), 51–83. https://doi.org/10.1109/PROC.1978.10837

Hikishima, M., Katoh, Y., & Kojima, H. (2014), Evaluation of waveform data processing in Wave-Particle Interaction Analyzer. *Earth Planets Space*, *66*, 63. https://doi.org/10.1186/s40623-018-0856-y

Hikishima, M., Kojima, H., Katoh, Y., Kasahara, Y., Kasahara, S., Mitani, T., et al. (2018), Data processing in the Software-type wave-particle interaction analyzer on board the Arase satellite. *Earth Planets Space*, *70*, 80. https://doi.org/10.1186/s40623-018-0856-y

Kasahara, Y., Kasaba, Y., Kojima, H., Yagitani, S., Ishisaka, K., Kumamoto, A., et al. (2018), The Plasma Wave Experiment (PWE) on board the Arase (ERG) satellite. *Earth, Planets and Space*, 70, 86. https://doi.org/10.1186/s40623-018-0842-4

Katoh, Y., Kojima, H., Hikishima, M., Takashima, T., Asamura, K., Miyoshi, Y., et al. (2018), Software-type Wave–Particle Interaction Analyzer on board the Arase satellite. *Earth Planets Space 70*, 4. https://doi.org/10.1186/s40623-017-0771-7

Kiyasu, Z. (1943), On A Design Method of Delay Networks (the original paper is written in Japanese). *The Journal of the Institute of Electrical Communication Engineers of Japan, 27*(8), 598–610.

Matsuda, S., Kasahara, Y., Kojima, H., Kasaba, Y., Yagitani, S., Ozaki, M., et al. (2018), Onboard software of Plasma Wave Experiment aboard Arase: instrument management and signal processing of Waveform Capture/Onboard Frequency Analyzer. *Earth, Planets and Space, 70*, 75. https://doi.org/10.1186/s40623-018-0838-0

Matsuda, S., Kojima, H., Kasahara, Y., Kasaba, Y., Kumamoto, A., Tsuchiya, F., et al. (2021), Direct antenna impedance measurement for quantitative AC electric field measurement by Arase. *Journal of Geophysical Research: Space Physics, 126*, e2021JA029111. https://doi.org/10.1029/2021JA029111

Mauk, B. H., Fox, N. J., Kanekal, S. G., Kessel, R. L., Sibeck, D. G., & Ukhorskiy, A. (2013), Science objectives and rationale for the radiation belt storm probes mission. *Space Science Reviews, 179*, 3–27. https://doi.org/10.1007/s11214-012-9908-y

Miyoshi, Y., Shinohara, I., Takashima, T., Asamura, K., Higashio, N., Mitani, T., et al. (2018), Geospace exploration project ERG. *Earth Planets Space, 70*, 101. https://doi.org/10.1186/s40623-018-0862-0

Nuttall, A. (1981), Some windows with very good sidelobe behavior. *IEEE Transactions on Acoustics, Speech, and Signal Processing, 29*(1), 84–91. https://doi.org/10.1109/TASSP.1981.1163506

Thomson, W.E. (1949), Delay Networks having Maximally Flat Frequency Characteristics. *Proceedings of the Institution of Electrical Engineers*, *Part III, Radio and communication engineering*, *96* (44), 487–490. https://doi.org/10.1049/pi-3.1949.0101

Tukey, J. W. (1967), An introduction to the calculations of numerical spectrum analysis. In B. Harris (Ed.), *Spectral Analysis of Time Series* (pp. 25–46). New York, NY: Wiley.

Tukey, J. W., & Hamming, R. W. (1949), *Measuring noise color 1*. Murray Hill, NJ: Bell Telephone Laboratories, Incorporated.

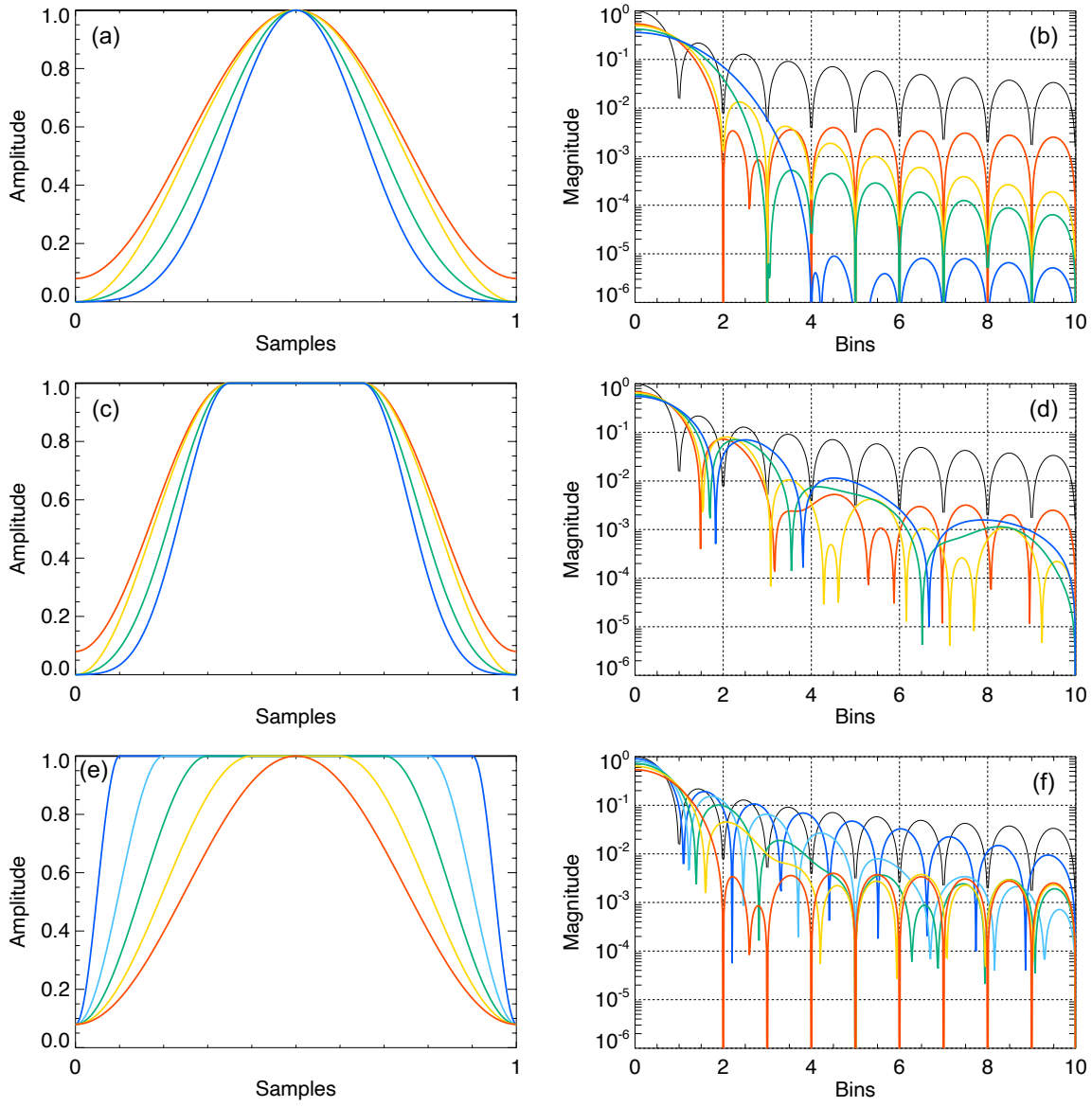

Figure 1. Summary plot of (a, c, and e) window functions and (b, d, and f) their frequency characteristics. (a, b) the cosine-sum windows: black, red, yellow, green, and blue lines correspond to the rectangular, Hamming, Hann, Blackman, and Blackman-Harris window, respectively. (c, d) the Tukey-type windows: black, red, yellow, green, and blue lines correspond to the rectangular, Tukey-Hamming, Tukey-Hann, Tukey-Blackman, and Tukey-Blackman-Harris window, respectively. All windows are plotted with $r = 0.3$. (e, f) the Tukey-Hamming windows: red, yellow, green, cyan, blue, and black lines correspond to $r = 0.0, 0.2, 0.4, 0.6, 0.8,$ and 1.0. respectively. $r = 0$ and 1 correspond to the normal Hamming window and the rectangular window, respectively.

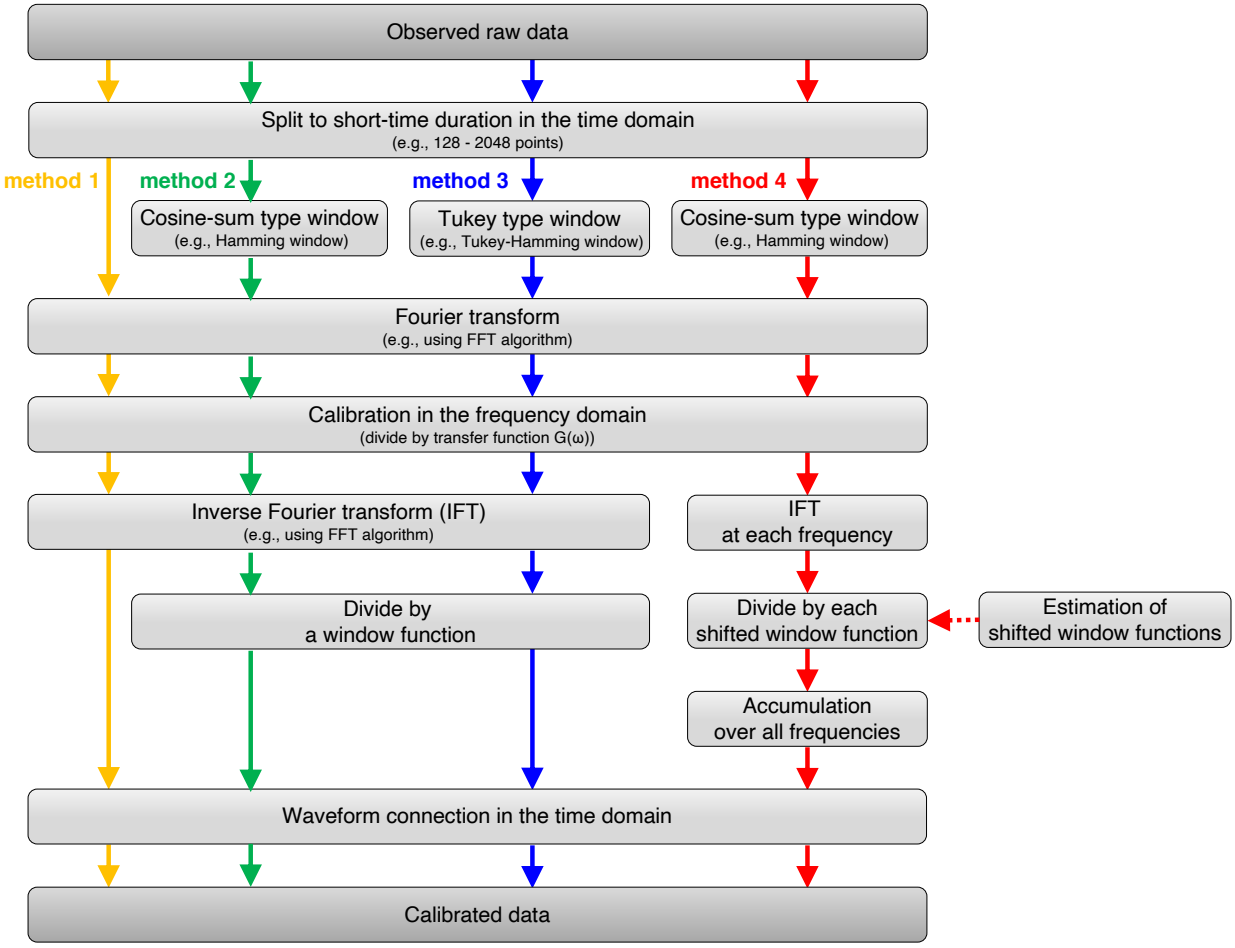

Figure 2. Flowchart of the calibration procedures for the STFT case comprising conventional methods (Method 1 (yellow), 2 (green), and 3(blue)) and the novel proposed method (Method 4 (red)).

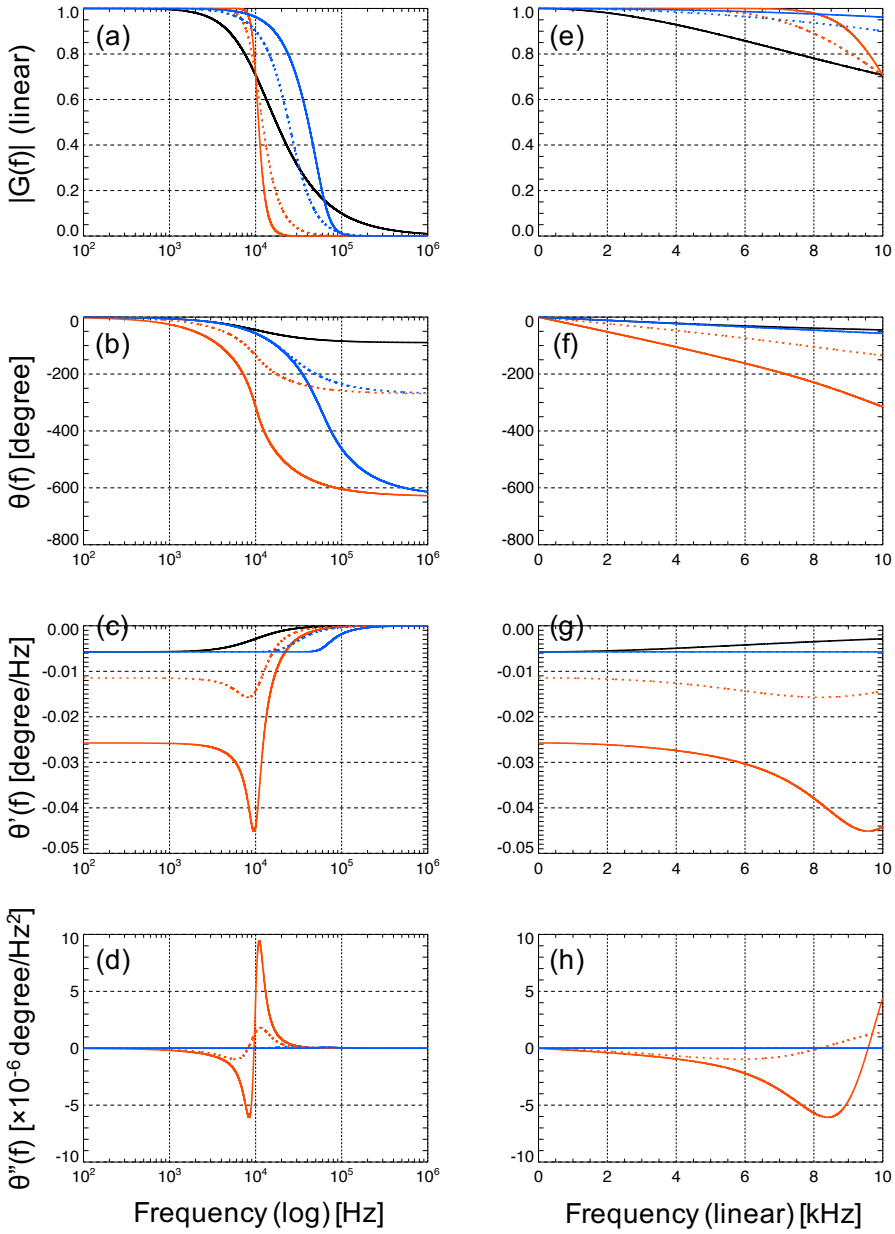

Figure 3. The properties of the filters with $f_{\text{cutoff}} = 10$ kHz and $G_0 = 1$. (a) and (e) are the amplitude components of the transfer function $|G(f)|$ corresponding to the gain of filters, (b) and (f) are phase components of the transfer function $\theta(f)$, (c) and (g) are the first-order derivatives of $\theta(f)$, (d) and (h) are the second-order derivatives of $\theta(f)$, respectively. Black lines, red lines, and blue lines correspond to the RC1, the Butterworth, and the Bessel filters, respectively, and dashed and solid red and blue lines correspond to the third- and seventh-order filter, respectively.

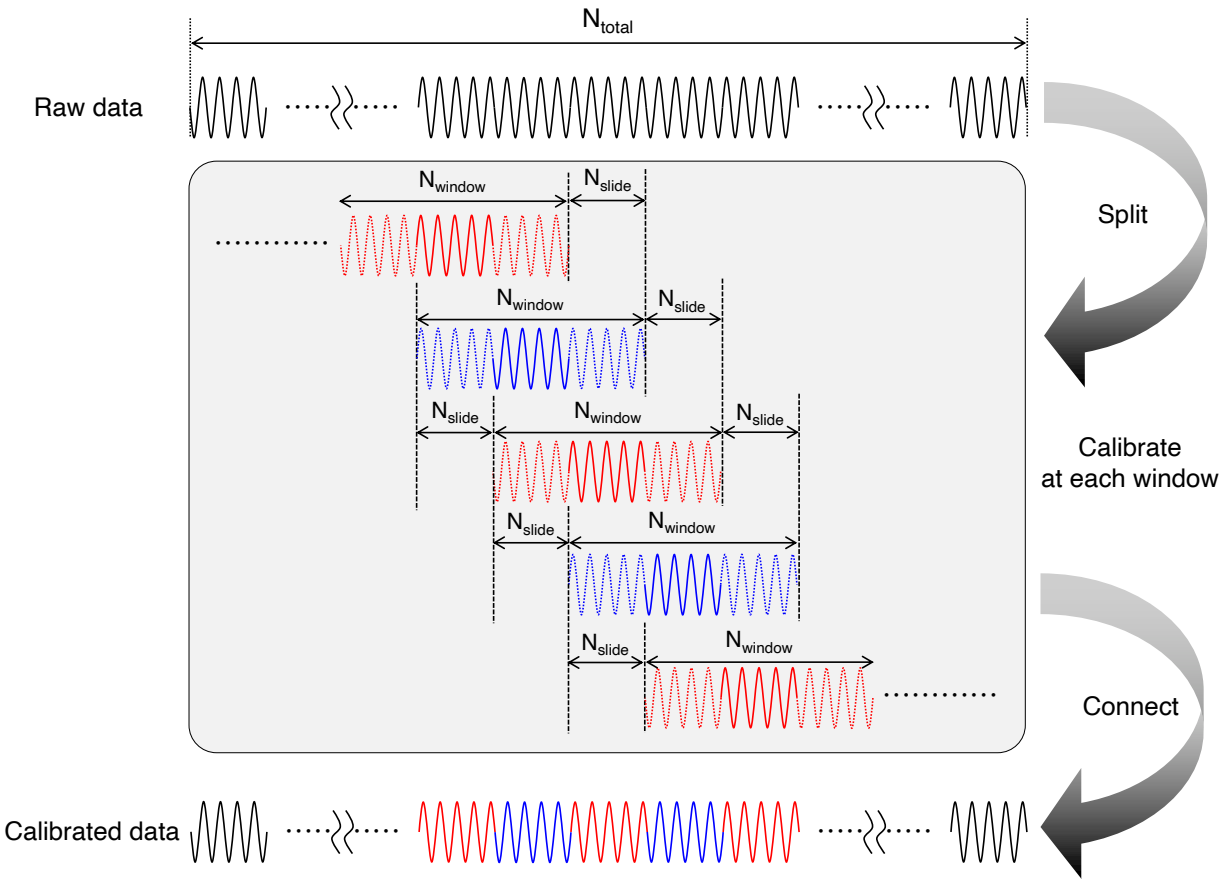

Figure 4. Schematic illustration of an STFT process and the definition of N_{window}, N_{slide}, and N_{total}.

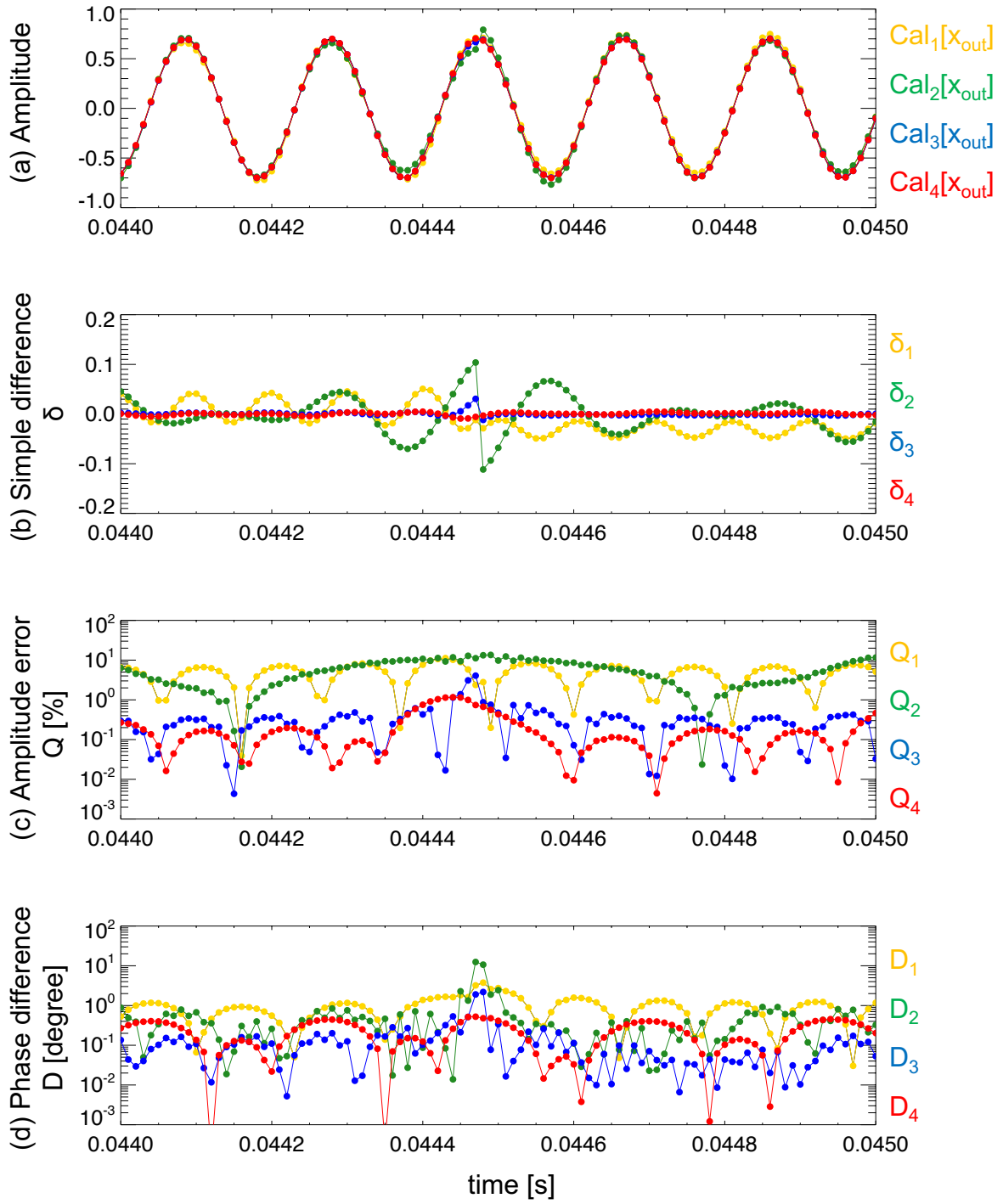

Figure 5. Sample plot of (a) $\mathcal{C}al_h[x_{\text{out}}(t_n)]$, (b) δ_h, (c) $Q_h(t_n)$, and (d) $D_h(t_n)$ for the third-order Butterworth filter with $f_s = 100$ kHz, $N_{\text{total}} = 10,000$, $T_{\text{total}} = 0.1$ s, $N_{\text{window}} = 128, N_{\text{slide}} = 64, f_{\text{in}} = 5.17$ kHz. The data around center are plotted. The yellow, green, blue, and red points and lines correspond to Method 1, 2, 3, and 4, respectively. Note that the input amplitude is 0.7.

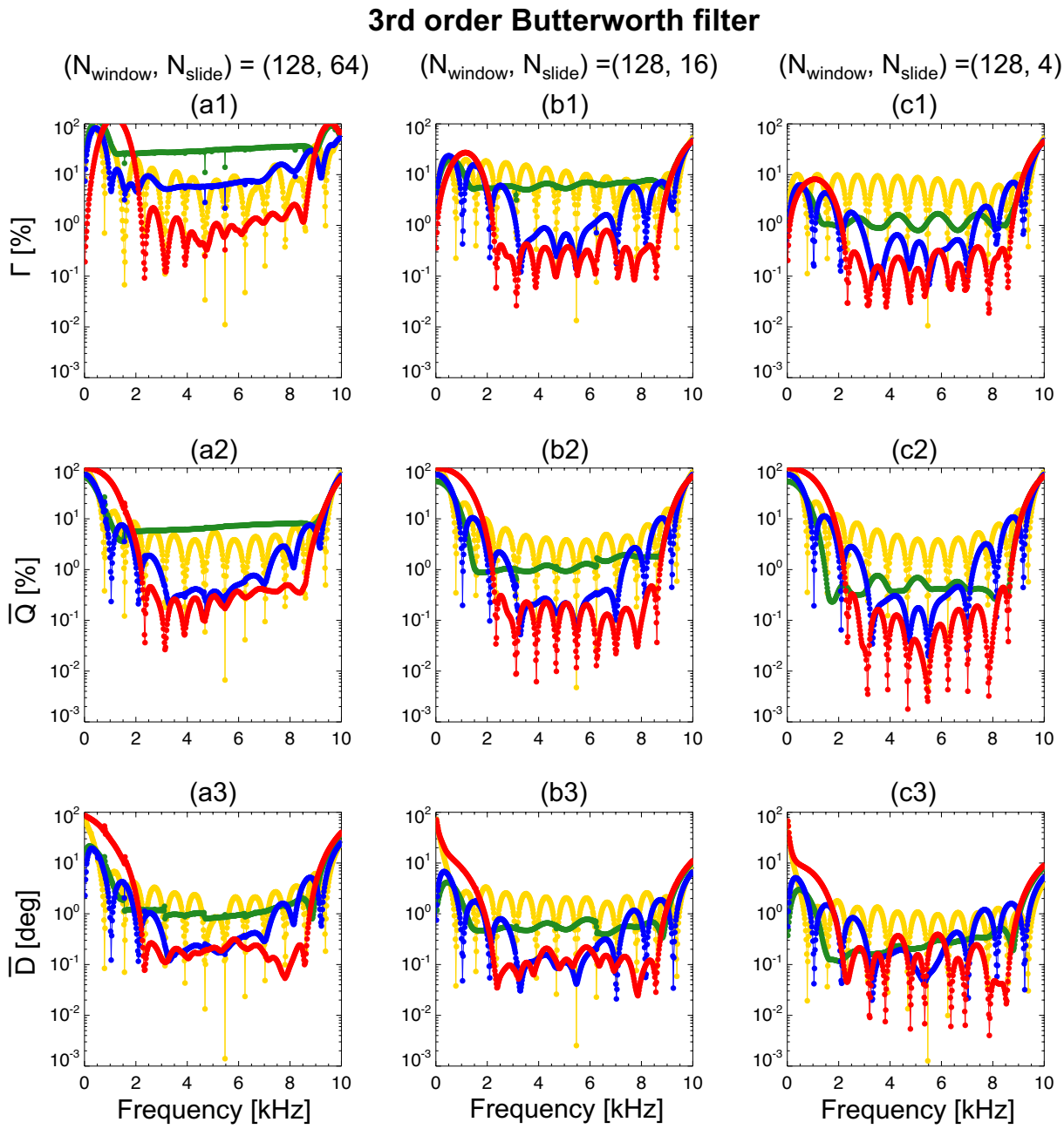

Figure 6. The frequency dependences of Γ_h, $\bar{Q}_h$, and $\bar{D}_h$ for the third-order Butterworth filter. (a1-a3) $(N_{\text{window}}, N_{\text{slide}}) = (128, 64(= N_{\text{window}}/2))$, (b1-b3) $(N_{\text{window}}, N_{\text{slide}}) = (128, 16(= N_{\text{window}}/8))$, (c1-c3) $(N_{\text{window}}, N_{\text{slide}}) = (128, 4(= N_{\text{window}}/32))$. The color format is the same as that of Figure 5.

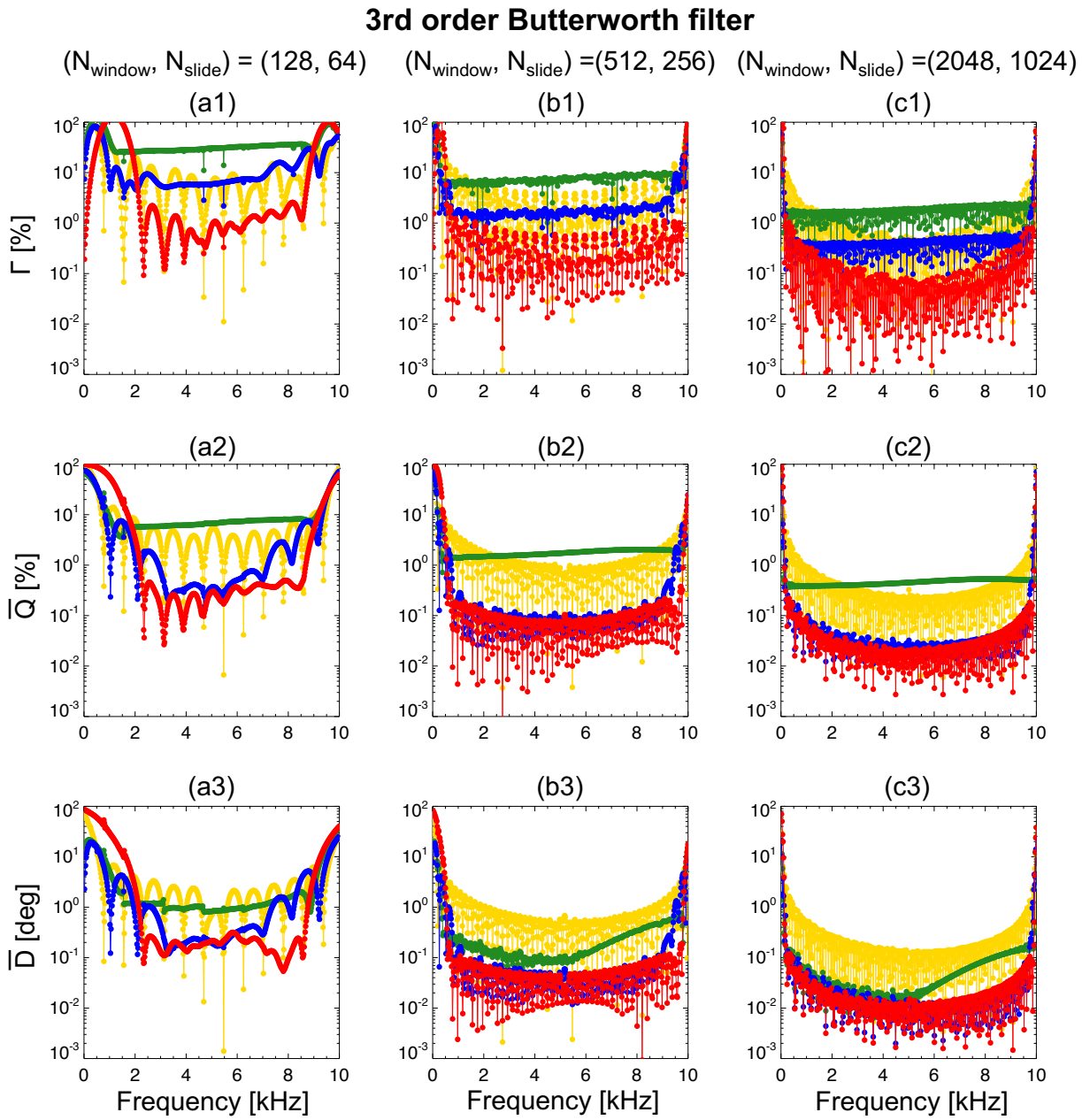

Figure 7. The frequency dependences of Γ_h, $\bar{Q}_h$, and $\bar{D}_h$ for the first-order RC filter. (a1-a3) $N_{\mathrm{window}} = 128$, (b1-b3) $N_{\mathrm{window}} = 512$, and (c1-c3) $N_{\mathrm{window}} = 2048$ with $N_{\mathrm{slide}}/N_{\mathrm{window}} = 0.5$. The color format is the same as that of Figures 5 and 6.

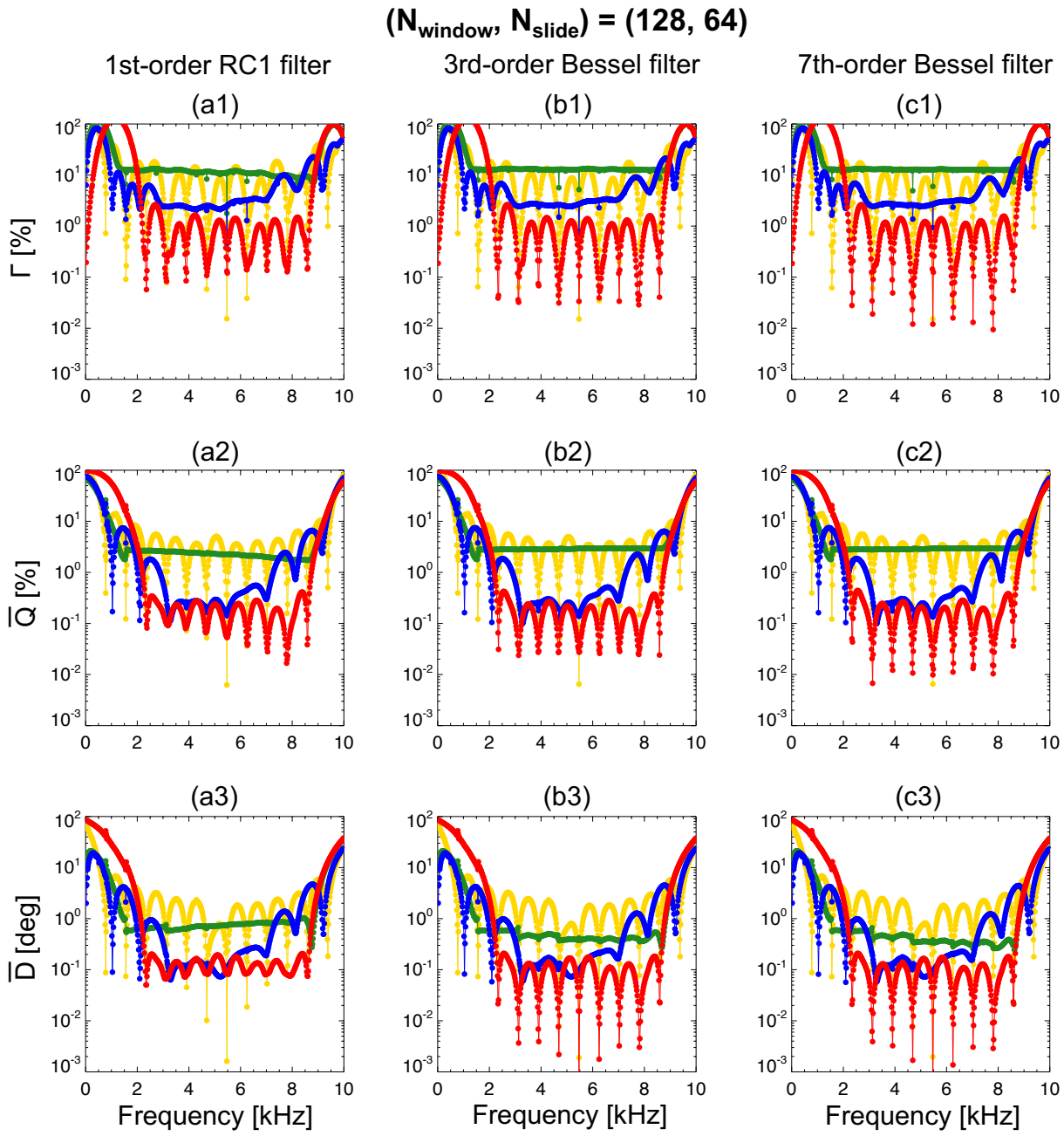

Figure 8. The frequency dependences of Γ_h, $\bar{Q}_h$, and $\bar{D}_h$ with $(N_{\mathrm{window}}, N_{\mathrm{slide}}) = (128, 64)$ for (a1-a3) the first-order RC filter, (b1-b3) the third-order Bessel filter, (c1-c3) the seventh-order Bessel filter. The color format is the same as that of Figures 5, 6, and 7.

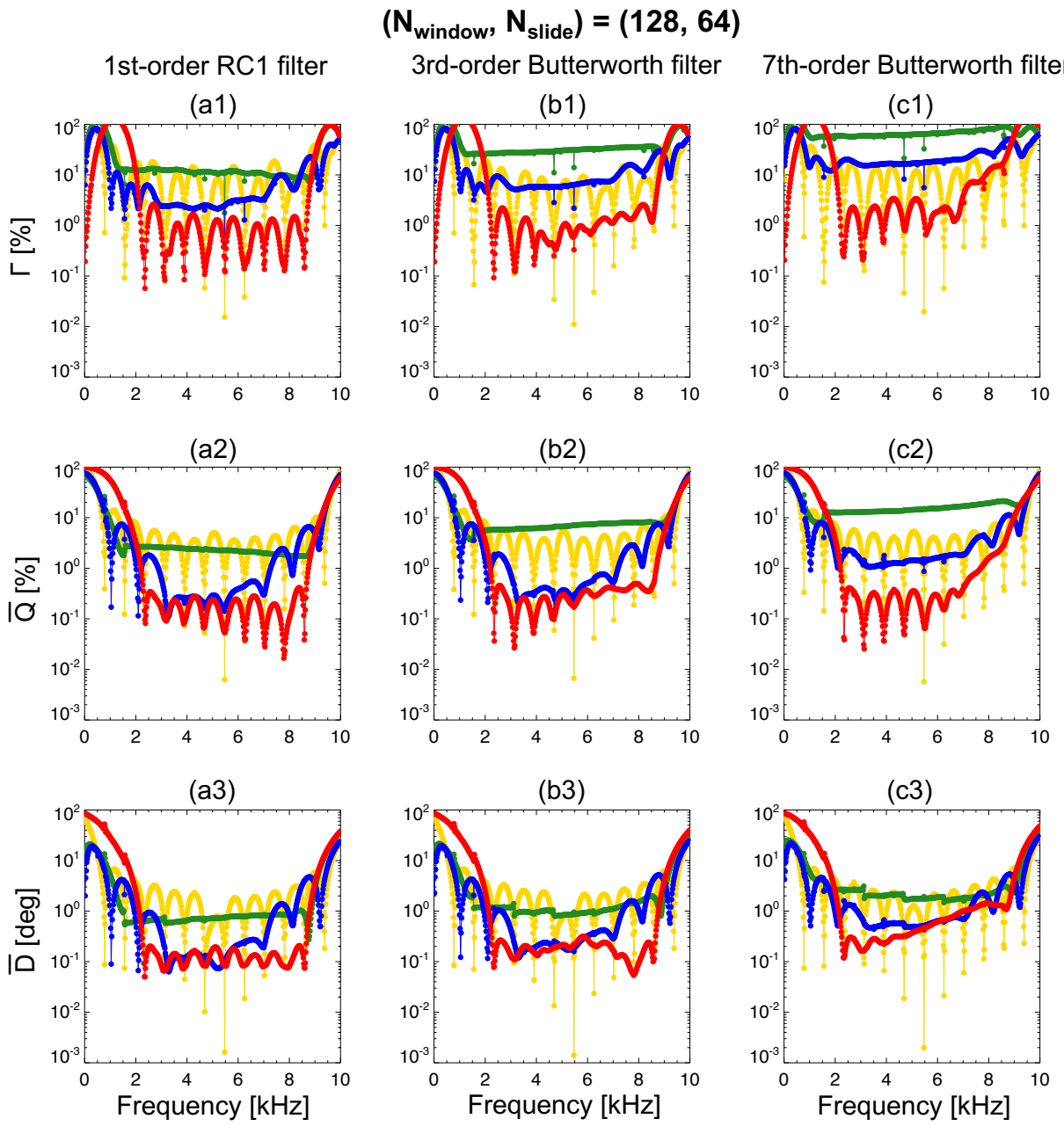

Figure 9. The frequency dependences of Γ_h, $\bar{Q}_h$, and $\bar{D}_h$ with $(N_{\text{window}}, N_{\text{slide}}) = (128, 64)$ for (a1-a3) the first-order RC filter, (b1-b3) the third-order Butterworth filter, and (c1-c3) the seventh-order Butterworth filter. The color format is the same as that of Figures 5, 6, 7, and 8.

675
676 **Table 1.** Summary of characteristics of each calibration method. N_{t}, N_{w}, N_{s}, and $\mathrm{ld}(x)$
677 represent N_{total}, N_{window}, N_{slide}, and the binary logarithm function, respectively.
678

	Method 1	**Method 2**	**Method 3**	**Method 4** (Our proposed method)
For removing side-lobe effect	Poor	Excellent	Good	Excellent
For removing main lobe effect	Excellent	Poor	Good	Excellent
Accuracy	Poor (Sometimes Excellent)	Poor	Good	Excellent
Seamlessness	Poor	Poor	Good (Sometimes Poor)	Excellent
Calculation time	$\mathcal{O}\left(\frac{N_{\mathrm{t}}N_{\mathrm{w}}\mathrm{ld}(N_{\mathrm{w}})}{N_{\mathrm{s}}}\right)$	$\mathcal{O}\left(\frac{N_{\mathrm{t}}N_{\mathrm{w}}\mathrm{ld}(N_{\mathrm{w}})}{N_{\mathrm{s}}}\right)$	$\mathcal{O}\left(\frac{N_{\mathrm{t}}N_{\mathrm{w}}\mathrm{ld}(N_{\mathrm{w}})}{N_{\mathrm{s}}}\right)$	$\mathcal{O}\left(\frac{N_{\mathrm{t}}N_{\mathrm{w}}^2}{N_{\mathrm{s}}}\right)$

679